APPLIED SCIENCES AND ENGINEERING

Tuning, optimization, and perovskite solar cell device integration of ultrathin poly(3,4-ethylene dioxythiophene) films via a single-step all-dry process

Meysam Heydari Gharahcheshmeh[1], Mohammad Mahdi Tavakoli[2], Edward F. Gleason[1], Maxwell T. Robinson[1], Jing Kong[2], Karen K. Gleason[1]*

For semicrystalline poly(3,4-ethylene dioxythiophene) (PEDOT), oxidative chemical vapor deposition (oCVD) enables systematic control over the *b*-axis lattice parameter (π-π stacking distance). Decreasing the *b*-axis lattice parameter increases the charge transfer integral, thus enhancing intracrystallite mobility. To reduce the barrier to intercrystallite transport, oCVD conditions were tailored to produce pure face-on crystallite orientation rather than the more common edge-on orientation. The face-on oriented oCVD PEDOT with the lowest *b*-axis lattice parameter displayed the highest in-plane electrical conductivity (σ_{dc} = 2800 S/cm), largest optical bandgap (2.9 eV), and lowest degree of disorder as characterized by the Urbach band edge energy. With the single step oCVD process at growth conditions compatible with direct deposition onto flexible plastic substrates, the ratio σ_{dc}/σ_{op} reached 50. As compared to spun-cast PEDOT:polystyrene sulfonate, integration of oCVD PEDOT as a hole transport layer (HTL) improved both the power conversion efficiency (PCE) and shelf-life stability of inverted perovskite solar cells (PSC).

INTRODUCTION

Optoelectronic, energy, and sensing devices envisioned in wearable form include organic photovoltaics (OPVs), organic light-emitting diodes, batteries, supercapacitors, thermoelectrics, and biosensors (*1*–*6*). Fabrication schemes for these next-generation devices motivate the development of highly electrically conducting thin layers, which are also lightweight, breathable, and mechanically flexible. In some cases, optical transparency is also essential. Many flexible substrates—such as plastics, papers, and textiles—are only compatible with mild fabrication conditions. While most flexible electrodes have been grown at high substrate temperatures, costly and complex transfer steps are required to integrate them with flexible substrates. For breathability, the spaces in fibrous substrates must remain open, requiring conformal coverage rather than blanket coating.

The requirements above have driven research on the oxidative chemical vapor deposition (oCVD) of conducting polymers (CPs) (*2*). In this powerful method, polymerization, doping, and thin-film formation occur simultaneous to conformally cover even nanostructured materials. The mild fabrication conditions permit direct deposition of conducting layers onto thermally sensitive substrates, including the leaves of plants (*7*). The oCVD films enabled OPVs fabrication directly on ordinary paper and plastic (*8*) and supercapacitor formation directly on paper and polymeric membranes (*9*). As desired for commercialization, uniform, defect-free, and ultrathin (<100 nm) oCVD CP films can be readily fabricated directly onto large-area (>600 cm^2) substrates by oCVD (*10*).

For oCVD, a monomer, such as 3,4-ethylene dioxythiophene (EDOT), is introduced into a hot-wall vacuum chamber as a vapor (Fig. 1). The monomer vapor, along with the oxidant vapor, adsorbs onto a cooler growth stage, where polymerization proceeds by a step-growth mechanism. Commonly, the oCVD oxidant consists of vapor iron (III) chloride (*11*–*16*), produced via the sublimation of solid $FeCl_3$ (Fig. 1A). In this case, the unreacted oxidants and many of the oxidation by-products have low volatility and do not desorb during the growth of the CP layer. To remove these species, a postdeposition rinsing step—using methanol (MeOH), hydrochloric acid (HCl), or hydrobromic acid (HBr)—can be used to improve film properties, such as electrical conductivity and optical transparency (*2*). However, the wet chemistry required rinsing; thus, the additional processing step, which rinsing represents, reduces the attractiveness of the oCVD approach using solid $FeCl_3$. True single-step, all-dry oCVD synthesis (Fig. 1B) can be achieved with more volatile oxidants, which are liquids under ambient conditions, such as Br_2 (*17*), $VOCl_3$, or $SbCl_5$ (*18*, *19*). In addition, the control over the delivery of reactants to growth surface is greatly enhanced by the volatile oxidants. In this work, all films are synthesized with $VOCl_3$.

In CPs, the doping process generates polarons (quasiparticles consisting of charge and phonon clouds) or bipolarons, which leads to electron delocalization over the backbone and facilitates the electronic conductivity. Anions derived from the oxidant, such as Cl^- or Br^-, incorporate into the oCVD films during growth, providing doping simultaneously with the film deposition. The resulting doped and conjugated poly(3,4-ethylene dioxythiophene) (PEDOT) chains have a linear structure with a tendency to form a semicrystalline matrix. The axis of π-π interchain stacking of the crystallites can be either parallel or orthogonal to the substrate. In CPs, both metallic and hopping conduction have been reported. The more dominant the metallic contribution, the higher the electrical conductivity (*20*). In the metallic regime, the dc conductivity remains finite as temperature approaches 0 K, and the log-log plot of the reduced activation energy ($w = \frac{\Delta \ln \sigma}{\Delta \ln T}$) versus temperature exhibits a positive slope at low temperature that confirms the existence of delocalized sates at the Fermi level in the metallic regime. The chain alignment and doping level (oxidation level) significantly affect the resulting electrical conductivity. Conductivity is also a function of intrachain, interchain, and intercrystallite charge carrier mobility. Carrier transport in CPs deviates from metallic conductivity due to the presence of disorder, which induces notable scattering of the charge carriers and

[1]Department of Chemical Engineering, Massachusetts Institute of Technology, 77 Massachusetts Avenue, Cambridge, MA 02139, USA. [2]Department of Electrical Engineering and Computer Science, Massachusetts Institute of Technology, 77 Massachusetts Avenue, Cambridge, MA 02139, USA.
*Corresponding author. Email: kkg@mit.edu

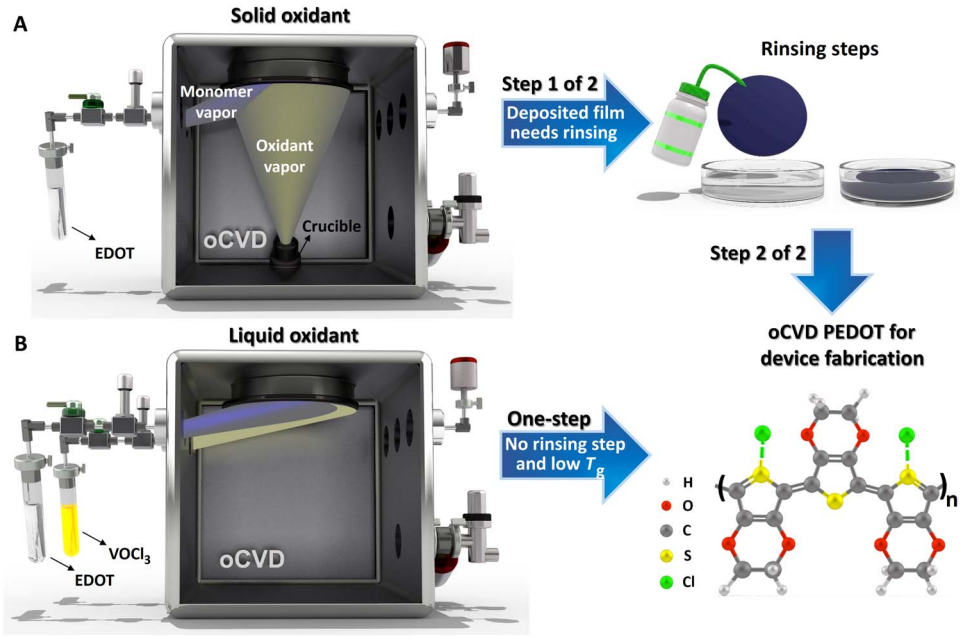

Fig. 1. Schematic illustration of PEDOT synthesis by the oCVD method. (**A**) The postdeposition acidic rinsing step (e.g., MeOH or HBr rinsing) is generally used for poly(3,4-ethylene dioxythiophene) (PEDOT) films grown using $FeCl_3$ as an oxidant to remove unreacted oxidants and oxidation by-products and increasing conductivity. (**B**) Synthesizing PEDOT using $VOCl_3$ as an oxidant does not require the acidic rinsing treatment, and the fabricated film is directly used in device fabrication as a true single-step, all-dry process.

leads to loss of extended states, known as Anderson localization (*21*). The type of disorder in CPs can be classified by comparison of the crystalline domain size ($L_{structure}$) and the extent of the localized wave functions of charge carrier ($L_{localization}$). In the homogenous disorder ($L_{structure} < L_{localization}$), the average electronic coupling of interchain among nanoscale one-dimensional (1D) chains is considered to be critical for the 3D conduction. In the inhomogeneous disorder ($L_{structure} > L_{localization}$), the intergrain coupling of granular metals (which are composed of metallic domains) surrounded by the low-conducting amorphous matrix is the crucial factor (*22*, *23*).

The high electrical conductivity along with the high optical transparency of PEDOT in the visible light regime is necessary for the application in organic optoelectronic devices such as solar cells. Multiple reports demonstrate improved OPV performance resulting from integration of the oCVD PEDOT layers (*2*). In the past few years, organic-inorganic perovskite materials with a chemical structure of ABX_3 (A: methylammonium, formamidinium, cesium, etc.; B: Pb, Sn, etc.; and X: I, Br, and Cl) have attracted tremendous attention of researchers due to their promising optoelectronic properties such as high diffusion length and mobility, ease of fabrication, and low-cost solution processing (*24*–*26*). These excellent properties render perovskites as ideal candidates for solar cell application. However, commercialization of a perovskite solar cell (PSC) requires further advancement in both power conversion efficiency (PCE) and long-term stability, along with low-cost materials and ease of large-scale production by processes such as roll to roll. The impact of integrating oCVD PEDOT with PSC devices is as yet unexplored.

To date, the optoelectronic performance of flexible electrodes has lagged that of brittle indium tin oxide (ITO). The figure of merit (FoM) for a transparent conductor is defined as the ratio of the dc electrical conductivity to the optical conductivity (σ_{dc}/σ_{op}) at a wavelength of 550 nm. Here, using a one-step, all-dry process compatible with the direct deposition onto most plastic substrates (growth temperature, ≤140°C), we obtained the FoM of 50 for oCVD PEDOT, which exceeds the benchmark indicator of the commercial viability of transparent conductor such as ITO (FoM, 35). This optimization is the direct result of the impressive ability to use systematic changes under the oCVD processing conditions to tune PEDOT film characteristics, including crystal texture, π-π interchain stacking distance, and bandgap. The presence of pure face-on orientation and lowering the *b*-axis lattice parameter by engineering the dopant level are of essential importance for enhancing electrical conductivity. Here, we report the observation of obtaining pure face-on orientation at temperatures compatible with plastic substrates that is the uniqueness of using volatile liquid oxidant. In addition, we systematically investigate the effect of oxidant saturation ratio (OSR) on the optoelectronic characteristics of PEDOT that is the first of its kind. In addition, we exhibit the critical impact of *b*-axis lattice parameter (π-π stacking distance) by engineering the dopant level on the electrical conductivity of the pure face-on–oriented oCVD PEDOT thin films. The tunability of the optoelectronic properties of oCVD PEDOT provides favorable band alignment between dissimilar layers in solar cell devices. Optimized oCVD PEDOT was successfully integrated as a hole transport layer (HTL) into an inverted PSC device. Compared to an identical structure with PEDOT:polystyrene sulfonate (PEDOT:PSS) as an HTL, the PCE of the PSC device incorporating the oCVD PEDOT was substantially improved (18.04% versus 16.2%). In addition, stability performance of inverted PSC over 42 days was significantly improved by the choice of an oCVD PEDOT HTL.

RESULTS AND DISCUSSION

For multiple reasons, the step growth polymerization of PEDOT is hypothesized to be a surface process (*1*, *2*). First, dimers and higher oligomers of EDOT have extremely low vapor pressure. In addition, the charged species that are intermediates in the oxidative polymerization

mechanism are energetically difficult to maintain in the gas phase. Furthermore, at low pressures, elementary gas-phase reactions involving two or more molecules are slow.

The saturation ratio, P/P_{sat}, determines the equilibrium surface concentration of the reactants, where P and P_{sat} are partial pressure and saturation pressure, respectively. In this work, the surface concentration of the volatile oxidant, $VOCl_3$, and the surface growth temperature are the primary variables for the oCVD PEDOT film synthesis, while EDOT monomer concentration on the surface was held at fixed levels. The calculated saturation ratio of EDOT monomer was 30,000 and 10,000 ppm (parts per million) at the growth temperature of 110° and 140°C, respectively. The experimental details, including the process of calculating monomer and OSRs, are provided in the Supplementary Materials (section S1, fig. S1, and table S1). The growth temperature and OSR, at the fixed monomer saturation ratio, significantly influence the polymer deposition rate and film thickness. It was noted that an increase in the OSR, as well as a decrease in growth temperature, induces the rise of film thickness and polymer deposition rate (fig. S2).

The structure and crystallization orientation of PEDOT films profoundly affect their electrical and optical characteristics. The ordered self-organization crystalline domains in many conjugated conducting and semiconducting polymers are surrounded by amorphous matrix. Here, grazing incidence x-ray diffraction (GIXRD) elucidates the structure of as-deposited PEDOT films with no additional rinsing treatment (e.g., HBr, HCl, or MeOH). The normalized GIXRD patterns reveal that the PEDOT films have excellent ordered structures, while their preferential crystallization orientation is strongly affected by the growth temperature and the OSR (Fig. 2A). The diffraction of (100) plane at $2\theta \sim 6.4°$ corresponds to an edge-on stacking orientation (h00), while the (020) plane at $2\theta \sim 25.5°$ corresponds to a face-on stacking orientation (0k0). The self-organization of PEDOT is reported in an orthorhombic structure, while a stacked lamellar structure with 2D conjugated sheets formed by interchain π-π stacking (*27*). The conjugated backbone is parallel to the substrate in both face-on and edge-on orientation. However, the π-π interchain stacking orientation is perpendicular to the plane of substrate in face-on orientation (Fig. 2B), while it is parallel to the plane of substrate in edge-on orientation (Fig. 2C).

The effect of the OSR and growth temperature on the crystallization orientation of all 16 oCVD PEDOT films (fig. S3) is summarized in Fig. 2D. The lengths of the red and blue bars exhibit the percentages of the face-on and edge-on orientation, respectively. To visualize the intensity of both face-on and edge-on peaks, we converted the integrated peak intensity of (100) and (200) to the equivalent integrated peak intensity of (020) using the Lorentz polarization (LP) factor, which is defined as $LP(\theta) = \frac{1+\cos^2(2\theta)}{\sin^2(\theta)\cos(\theta)}$ (*28*). A detailed discussion is provided in section S2 and table S2. All PEDOT films grown at the deposition temperature of 140°C have essentially pure face-on orientation (Fig. 2D). The crystallization orientation of PEDOT films grown at 110°C shows pure face-on orientation when the OSR is less than 630 ppm, and gradually, the percentage of edge-on orientation increases from 1 to 16% by an increase in OSR from 630 to 1260 ppm. It is postulated that the increase in film thickness to more than 130 nm (fig. S2) also influences the appearance of edge-on orientation in film grown at the deposition temperature of 110°C, while the films grown at the deposition temperature of 140°C at all oxidant levels display pure face-on orientation independent of film thickness. In general, it can be concluded that the PEDOT films grown at the higher growth temperatures and lower OSR result in an in situ reorganization to a face-on orientation.

The crystallization orientation of conjugated polymers leads to anisotropy in charge transport parallel and perpendicular to the conjugation direction. High in-plane carrier mobility and electrical conductivity have been widely reported in conjugated polymers (both p-type and n-type) with face-on orientation (*29*–*33*) due to the low energy barrier of intercrystallite charge transport. When the electrical conductivity measured at given temperature, [$\sigma(T)$], is limited by intercrystallite transport (*34*)

$$\sigma(T) \propto \exp\left[-\left(\frac{W_\gamma}{k_B T}\right)^{\frac{1}{2}}\right] \quad (1)$$

where W_γ is the energy barrier of intercrystallite charge transport and k_B is the Boltzmann constant.

The intermolecular forces and polymer structure play a substantial role in crystallinity and amorphicity. The crystalline regions emerge from the high degree of π-orbital overlaps, whereas amorphous regions appear from weak interactions of random polymer chain orientations. The polymer chains can bridge the adjacent crystallites and act as tie chains without a notable conjugation loss as long as the molecular weight is high enough at the presence of sufficiently large density of ordered structures and few sp^3-coordinated carbon defects. In this case, one polymer chain belongs to several crystallites (*35*). The presence of extensive intergrain connectivity is postulated in the pure face-on orientation through bridging the neighboring grains by polymer chains (especially in a low-angle grain boundary regime) with the minimal distortion, which provides the electrical pathway across grain boundary. In such a case, a charge will likely find its way to an adjacent grain as the outcome of the transport barrier reduction. However, the presence of mixed face-on and edge-on orientations is postulated to provide high-angle grain boundaries (larger misorientations between neighboring crystallites with respect to polymer chain axis) and, thus, act as defects and barriers for transport. In addition to the mobility within the grain boundary (μ_{gb}), the mobility within the crystallite (μ_c) is another critical factor that needs to be considered and will be discussed later in this manuscript. The μ_{gb} is mainly attributed to the crystallization orientation, while the μ_c is highly lattice parameter dependent, and in general, μ_c is much larger than the μ_{gb} ($\mu_c >> \mu_{gb}$). Wang *et al.* (*29*) reported the presence of face-on orientation in ultrathin PEDOT films grown at the deposition temperature of higher than 200°C and after HBr acidic treatment while using $FeCl_3$ as an oxidizing agent. They attributed higher in-plane electrical conductivity and higher in-plane carrier mobility to the increase in preferred face-on orientation in PEDOT films. Figure 2E exhibits the reported crystalline orientation result of oCVD PEDOT film grown at the deposition temperature of 150°C while using $FeCl_3$ as an oxidizing agent (*29*). By comparing Fig. 2D and Fig. 2E, it can be noted that the use of $VOCl_3$ encourages the growth of the higher conductivity face-on orientation compared to its solid oxidant counterparts, even at lower temperature deposition. The presence of pure face-on orientation in films grown by $VOCl_3$ as an oxidant at the deposition temperatures compatible with most plastic substrates (≤140°C) brings the considerable advantage to increase the electrical conductivity at lower deposition temperature with no need of acidic rinsing treatment.

The mechanism of crystalline orientation changes with different oxidant is not yet fully understood. However, we hypothesize that at growth temperatures above PEDOT's glass transition temperature (T_g) of ~100°C (*36*), the crystalline orientation of the conjugated

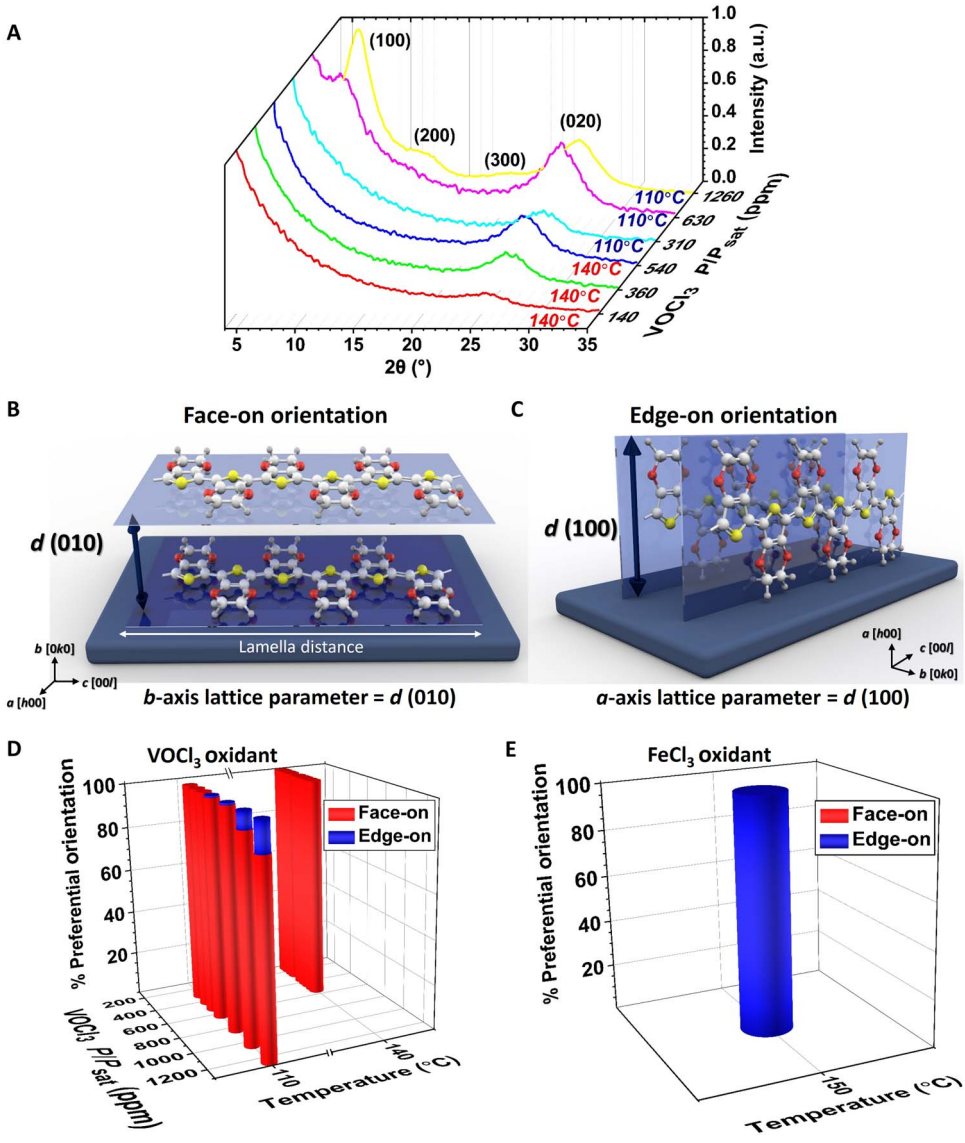

Fig. 2. Different crystallization orientation induced by process parameters. (**A**) The out-of-plane GIXRD θ – 2θ diffraction patterns of as-deposited PEDOT films grown on silicon substrates at the different deposition temperature of 110° and 140°C with varying $VOCl_3$ saturation ratio. a.u., arbitrary units. Schematic illustration of crystallization orientation and the distance between planes in (**B**) face-on orientation and (**C**) edge-on orientation. (**D**) Summary of the percentage of preferential crystallization orientation in the bar chart for all 16 PEDOT films grown at different deposition temperature and $VOCl_3$ saturation ratio. The percentage of preferential orientation was calculated on the basis of the normalized integrated peak intensities after applying the Lorentz polarization (LP) factor. The lengths of the red-colored and blue-colored bars display the percentage of the face-on and edge-on orientation, respectively. (**E**) The percentage of preferential crystallization orientation in PEDOT films grown at the deposition temperature of 150°C and using $FeCl_3$ as an oxidant as a comparison with the volatile liquid oxidant ($VOCl_3$) that is used in this study.

polymer is mainly related to intermolecular interaction and energy minimization of the film's matrix and interfaces during crystallization. The absence of oxidant by-products in films deposited by a volatile oxidant, $VOCl_3$ (fig. S4), compared to its solid oxidant counterpart, $FeCl_3$, is likely a critical factor that induces more dominant face-on orientation. We perfomed x-ray photoelectron spectroscopy (XPS) analyses to investigate the amount of oxidant by-product and evaluate the chemical composition of as-grown PEDOT films (fig. S4 and table S3). The absence of oxidant by-products was noticed in film grown at the deposition temperature of 140°C and the OSR value of 140 ppm, while there was no sign of nonionized impurities such as vanadium in the film. The vanadium atomic percentage was also negligible in the range of 0.06 and 0.13% for films grown at the OSR value of 140 and 360 ppm, respectively. The presence of oxidant by-products not only influences the crystalline orientation but also can inhibit crystal formation. The elemental analysis exhibits that the ratio of chlorine/sulfur (Cl/S), which is an indication of doping level, increases from 0.31 to 0.69 with an increase in OSR from 140 to 560 ppm. The high amount of Cl-doping level (e.g., >1/3) is also reported by Lee *et al.* (*37*) in oCVD PEDOT films grown by $FeCl_3$.

The quality and tunable nature of vapor-phase polymerization by oCVD method bring the extraordinary advantage to control the lattice parameter and crystalline orientation based on the device applications. The pure face-on orientation achieved in this oCVD

processing using the $VOCl_3$ oxidant is difficult to achieve in liquid-applied PEDOT:PSS or PEDOT synthesized by other methods.

The PEDOT crystallite size is calculated from the full width at half maximum of the diffraction peaks using the Scherrer equation (*38*). Films grown using the $VOCl_3$ oxidant at surface temperatures of 110° and 140°C have limited variation in crystallite sizes (details in section S2 and table S4). As will be discussed later, these films displayed a large variation in electrical conductivity. This suggests that charge transport within the crystallites does not limit overall film conductivity. For the face-on crystallites, the mean crystallite size was 3.2 nm. A similar value, 3.0 nm, was previously reported for films grown with $FeCl_3$ as the oxidant (*30*). The same comparison for the edge-on crystallite size gives a slightly larger value, 6.5 nm, with the current $VOCl_3$ oxidant versus 5.5 nm with the previous $FeCl_3$ oxidant. Although enhanced charge mobility is likely within these larger crystallites, their overall film conductivity of the edge-on films is lower, again supporting the hypothesis that intracrystalline charge transport is not dominating the measured in-plane conductivity in these films. Thus, the crystallite size analysis supports the hypothesis that the intercrystallite transport (Eq. 1) is likely the dominating factor for the electrical conductivity of this set of oCVD films.

For the PEDOT films deposited at 110° and 140°C, the *b*-axis lattice parameters increase as a function of the OSR for $VOCl_3$ (Fig. 3A, section S2, and table S5). At higher OSR, larger *b*-axis lattice parameters reveal a rise in dopant level that induces a stretch in π-π interchain stacking. The increase in dopant level by increase in OSR (table S3) is also consistent with the observed reduction of optical bandgap (E_g) values, which will be discussed later in this manuscript. Similarly, the *a*-axis lattice parameter increases with increasing OSR (fig. S5). The obtained *b*-axis lattice parameter of PEDOT grown by volatile liquid oxidant ($VOCl_3$) is higher (approximately >0.1 Å) than the previous x-ray studies of oCVD PEDOT grown by a solid oxidant such as $FeCl_3$ (*29*, *36*), which is an indication of higher doping level of these samples compared to their counterparts grown by solid oxidant.

The in-plane electrical conductivity decreases systematically with an increase in the *b*-axis lattice parameter (Fig. 3B). The lower OSR induces the lower *b*-axis lattice parameter (Fig. 3A) and correlates with the higher electrical conductivity (Fig. 3B). On the basis of the Drude model ($\sigma = qn\mu$, where q is unit of charge), σ is a function of both carrier density (n) and carrier mobility (μ). Achieving high μ in the presence of high n is challenging and needs perfect control on crystallinity and orientation of CPs to avoid scattering due to the ionized impurity scattering, which is induced by increasing the dopant level. The improvement of carrier mobility by decreasing the *b*-axis lattice parameter in terms of charge transfer integral will be discussed later in this manuscript. The electrical conductivity of ~2800 S/cm was achieved in PEDOT film with pure face-on orientation and the *b*-axis lattice parameter of 6.97 Å. Note that this electrical conductivity was achieved in as-grown PEDOT film at a substrate temperature compatible with direct deposition onto plastic substrates (140°C). Because no postdeposition rinsing step is required (because of the absence of oxidant by-products), this $VOCl_3$ oCVD process is a true single-step, all-dry process. The reduction of electrical conductivity with the approximate range of 7 to 15% was noticed after MeOH rinsing, which correlates with the absence of oxidant by-products in as-grown PEDOT films using $VOCl_3$ oxidant (fig. S4). The obtained electrical conductivity of ~2800 S/cm is approximately 10 times higher than the previously reported value by Wang *et al.* (*29*) in PEDOT films grown at the deposition temperature of 150°C while using $FeCl_3$ as an oxidizing agent and using HBr acidic rinsing treatment. By comparing Fig. 2D and Fig. 2E, it can be noted that such a high electrical conductivity in PEDOT films grown by $VOCl_3$ as an oxidizing agent compared to its counterparts grown by $FeCl_3$ as an oxidant is mainly attributed to the pure face-on orientation.

The decrease in PEDOT *b*-axis lattice parameter through engineering of the dopant incorporation is an effective strategy to achieve high electrical conductivity. The reduction of *b*-axis lattice parameter induces a high degree of molecular packing and enhances the π-π interchain coupling, resulting in an increase in charge carrier mobility and yielding electrical conductivity enhancement. Our results indicate that the presence of (i) pure face-on orientation and (ii) low *b*-axis lattice parameter (short π-π stacking distance) in PEDOT films is of essential importance to enhance the electrical conductivity. Both the pure face-on orientation and the reduction of π-π stacking distance introduce geometric constraints that are hypothesized to increase the probability of a single conjugated chain bridging between crystallites.

The effects of one dimensionality of a polymer chain and disorder on the nature of metallic state and insulator-metal transition are still controversial issues, concerning the details of the charge transport mechanisms in CPs (*39*, *40*). The backward scattering of the delocalized Bloch waves [combination of plane wave by a periodic function in the form of $\psi(\mathbf{r}) = e^{i\mathbf{k}\cdot\mathbf{r}}u(\mathbf{r})$, where ψ is the Bloch wave, $\mathbf{r}$ is a position, u is a periodic function, and $\mathbf{k}$ is the crystal wave vector] by disorder, defects, impurities, and grain boundaries induces the localization of wave functions in CPs. The origin of the localization can be due to the passage of 1D chains through a disordered region (based on either homogenous or inhomogeneous model). In both disorder models, the interchain charge transfer (through interchain interaction) is of great importance for delocalization and hence controls the final metallic state. In the case of interchain packing through decreasing the *b*-axis lattice parameter in heavily doped CPs, there is an increased probability that an electron can diffuse to a neighboring chain before traveling between defects and chain breaks in which electron states are extended three-dimensionally and, hence, are metallic.

Long-range in-plane conductivity depends on the current transport between lamella and grain-to-grain transport. The presence of low-angle grain boundary with the extensive intergrain connectivity in pure face-on orientation (Fig. 2D) and short π-π stacking distance in heavily doped films with high electrical conductivity (Fig. 3B) leads to the hypothesis that conductivity is quasi-1D. Generally, the 3D conduction is eliminated in ultrathin films. The existence of quasi-1D conductivity in CPs correlates with the efficiently enhanced charge transport and electrical conductivity along a controllable direction. It should be pointed out that such a quasi-1D conductivity as the outcome of well interchain coupling in the form of metallic islands is different from conventional 1D conductivity, which consists of isolated chains. The schematic illustration of such a quasi-1D conductivity, as well as the importance of short π-π stacking distance in heavily doped CPs, is depicted in Fig. 3 (C and D). In these schematics, the conduction pathway parallel to the substrate requires charge transport to primarily occur (i) along chains that transverse multiple crystallites by bridging across amorphous regions and (ii) between chains in the crystalline region. Any interchain transport is presumed to be slow in the less dense amorphous regions. In the case that (ii) is rate limiting, in-plane conductivity would be determined by the overlap integral, which depends critically on the *b*-axis lattice parameter. An analogous concept is reported for organic superconductors, where the interchain distance decreases by applying pressure to

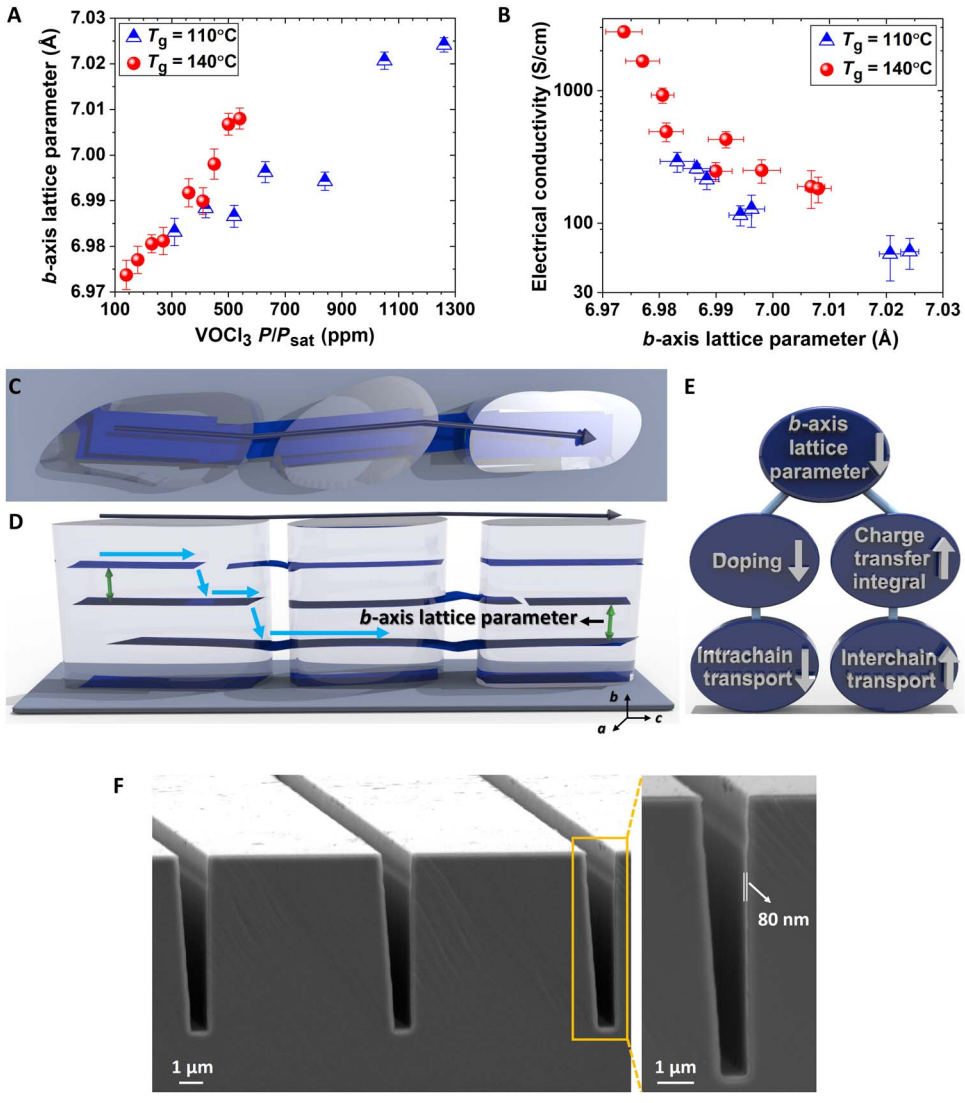

Fig. 3. Effect of PEDOT lattice parameter on electrical conductivity. (**A**) *b*-axis lattice parameter as a function of OSR in PEDOT films grown at the different deposition temperature of 110° and 140°C. (**B**) The relation of electrical conductivity and *b*-axis lattice parameter of PEDOT films grown at the different deposition temperature. (**C**) Schematic illustrations of possible current transport direction in the pure face-on orientation with low-angle grain boundaries. (**D**) Illustration of the high impact of low *b*-axis lattice parameter (short π-π stacking distance) and chain bridging to avoid localization in the pure face-on microstructure. The blue arrows display the direction of current flow. (**E**) Schematic illustration of *b*-axis lattice parameter influence on the intra- and interchain charge transport. The intrachain charge transfer was affected by the doping level, while the interchain charge transfer was influenced by the charge transfer integral. (**F**) Left: The cross-sectional scanning electron microscopy (SEM) image of the oCVD PEDOT film grown by $VOCl_3$ as an oxidant with a thickness of ~80 nm on a silicon wafer with etched trench structures demonstrating high conformality of the deposition. Right: The cross-sectional SEM image of the highly conformal oCVD PEDOT film on a trench with high magnification.

enhance and avoid disruption in the current flow by the concept of increasing the charge transfer integral (*41*).

The charge transfer integral (electronic coupling) is a critical parameter to enhance electrical conductivity and is directly associated with the carrier mobility and needs to be modulated in heavily doped CPs by interchain and intrachain arrangement. The interchain transfer integral ($t_\perp$) is one of the key parameters that governs the transport in conjugated polymers in the microscopic level and has chain distance exponential decay as (*42*)

$$t_\perp = t_0 \exp(-\gamma x) \tag{2}$$

where t_0 is the charge transfer integral at the minimum distance, x is the distance between chains (here, *b*-axis lattice parameter), and $1/\gamma$ is the wave function overlap decay length.

The charge transfer rate (k_{ij}) is based on the charge hopping theory and is proportional to the square of the interchain transfer integral ($t_\perp$) based on the semiclassical Marcus-Hush theory in organic materials (*42*–*44*)

$$k_{ij} = \frac{{t_\perp}^2}{\hbar}\sqrt{\frac{\pi}{\lambda k_B T}}\exp\left[-\frac{(\Delta E_{ij}+\lambda)^2}{4\lambda k_B T}\right] \tag{3}$$

where ħ is the reduced Planck constant; λ is the reorganization energy, which is related to molecule rearrangement and their surroundings during charge transfer; k_B is the Boltzmann constant; T is the temperature; and E_{ij} is the energy difference between nearby electronic states.

The carrier mobility is proportional to the square of the interchain transfer integral ($t_\perp$) and can be estimated using the Einstein equation (*44*)

$$\mu = \frac{eD}{k_B T} = \frac{e}{k_B T}\left(\frac{1}{2n}\sum_i d_i^2 k_i P_i\right) \quad (4)$$

where D is the charge diffusion coefficient given by $\left(\frac{1}{2n}\sum_i d_i^2 k_i P_i\right)$, e is the electronic charge, k_B is the Boltzmann constant, T is the temperature, n is an integer number and represents the system dimensionality, d_i is the center mass distance to neighbor i, P_i is the relative diffusion probability to a particular ith neighbor, and k_i is the charge transfer rate calculated according to Eq. 3.

As can be noted from Eqs. 2 to 4, the increase in carrier mobility and, thus, electrical conductivity enhancement at the constant temperature requires (i) the increase in charge transfer integral through *b*-axis lattice parameter reduction (which is satisfied in Fig. 3B) and (ii) reorganization energy reduction. The reorganization energy is the characteristic of a material and is not significantly affected by the lattice parameter variation. The obtained high in-plane electrical conductivity in pure face-on orientation (not a mixture of face-on and edge-on) in this study can also be interpreted by enhanced carrier mobility in terms of charge transfer integral. The transfer integral gradually decreases with the increase in tilt angle from cofacial orientation (*42*). The increase in electrical conductivity by decrease in *b*-axis lattice parameter can also be interpreted by the Miller-Abrahams equation (*45*), which is valid for weak electron-phonon coupling and low temperatures (section S3).

The charge transfer rate between nearest neighbor crystallites, "a" and "b," k_{ab} in ultrathin film of semicrystalline PEDOT is the sum of two parallel processes

$$k_{ab} = k_{ab}(\text{hopping}) + k_{ab}(\text{bridging}) \quad (5)$$

Under synthesis conditions where there is a reasonable probability that the length of a PEDOT exceeds the distance between crystallites, the rate of charge transport by the bridges dominates, and Eq. 5 reduces to $k_{ab} \sim k_{ab}(\text{bridging})$. In addition, we can postulate that the probability of bridges between non-neighboring crystallites can be neglected because there are few chains long enough to form these direct bridges. Hence, to have conductivity between non-neighboring crystallites, the charge would need to travel a path composed of $(N + 2)$ crystallites having $(N + 1)$ nearest-neighbor bridges. With this nomenclature, $N = 0$ is the nearest-neighbor case in which two crystallites are connected by one nearest-neighbor bridge (a ↔ b). Similarly, $N = 1$ is a ↔ b ↔ c, where "ab" and "bc" are nearest neighbors but "ac" is not, and $N = 2$ is a ↔ b ↔ c ↔ d, with only "ab," "bc," and "cd" as nearest neighbors.

The charge transfer happens in series inside the first crystallite, then across the first bridge, then inside the next crystallite, and then across the next bridge, following as

$$\frac{1}{k_{total}} = \frac{1}{k_a} + \frac{1}{k_{ab}} + \frac{1}{k_b} + \frac{1}{k_{bc}} + \frac{1}{k_c} + \ldots + \frac{1}{k_{(n-1)(n)}} + \frac{1}{k_n} \quad (6)$$

If the charge transfer rate across the bridges is fast relative to the transfer inside the crystals, i.e., $k_{ab} >> k_a$, then

$$\frac{1}{k_{total}} \sim \frac{1}{k_a} + \frac{1}{k_b} + \frac{1}{k_c} + \ldots + \frac{1}{k_n} \quad (7)$$

In the simplest case where $k_a = k_b = k_c = \ldots = k_n$ (i.e., equal charge transfer rates inside each crystallite), k is related to the *b*-axis parameter by the transfer integral. In the case, $\frac{1}{k_{total}} \sim \frac{N}{k}$ or

$$k_{total} \sim \frac{k}{N} \quad (8)$$

For a distribution of rates inside the crystallites, an integral could be performed instead. In general, lowering the *b*-axis lattice parameter in heavily doped PEDOT films in both metallic and hopping mechanisms (the more dominant the metallic contribution, the less amount of disorder in the system and the higher the electrical conductivity) is a promising approach for electrical conductivity enhancement. Figure 3E illustrates the summary of *b*-axis lattice parameter influence, due to the OSR variation, on the intra- and interchain charge transport. Several conduction mechanisms are occurring in series. The rate of charge transport along the chain is affected by the doping level. However, charge mobility along one given chain at any doping level exceeds the chain-to-chain transport. The interchain charge transfer, which is affected by charge transfer integral, is the rate-limiting step for the overall film conductivity. We believe that by further improvement of fabrication process parameters, the lower *b*-axis lattice parameter at even higher doping level can be achieved to further enhance the electrical conductivity.

Before going forward with the discussion of optical characteristics and photovoltaic (PV) device fabrication, the conformality of the PEDOT film with $VOCl_3$ as a volatile liquid oxidant was assessed by depositing a ~80-nm film grown at the deposition temperature of 140°C on a silicon wafer with etched trench structures. The vapor-phase polymerization thorough oCVD method enables the formation of highly conformal coating, as can be noted in Fig. 3F. The ability of vapor-phase reactants to diffuse into rough surfaces—including ordinary plastics, papers, textiles, and complex micro- and nanostructured surfaces to produce highly conformal films—is of great importance. The ability to achieve conformal coverage opens up promising routes for the design of novel high-performance optoelectronic devices. In addition, the low-temperature vapor-phase deposition approach allows integration directly onto materials that would be damaged by heat or solvents and thus enables additional cost-effective next-generation fabrication opportunities.

The low sheet resistance and high optical transmittance of CPs are of essential importance for application as transparent electrodes. There is typically a trade-off between transparency and sheet resistance. Therefore, the FoM (FoM = σ_{dc}/σ_{op}, where σ_{dc} and σ_{op} are dc conductivity and optical conductivity, respectively) is defined to assess the property of a transparent electrode. Transmittance and sheet resistance are related on the basis of the following equation (*2*, *46*, *47*)

$$T = \left(1 + \frac{Z_0}{2R_{sh}}\frac{\sigma_{op}}{\sigma_{dc}}\right)^{-2} \quad (9)$$

where T is the transmittance value at λ = 550 nm, $Z_0 = 377$ ohms is the impedance of free space, and R_{sh} is the sheet resistance.

To minimize the contribution of morphology to the observed results, the study of optical properties focused on the series of oCVD PEDOT produced with the $VOCl_3$ oxidant at a fixed deposition temperature of 140°C. The OSR ratio varied from 140 to 540 ppm. These films all have pure face-on orientation and crystallite sizes within ~8% of the mean value. An optical photograph of this series of films deposited on glass slide substrates is shown in Fig. 4A. The ultraviolet-visible–near-infrared (UV-vis–NIR) spectra of films are shown in Fig. 4B. The highest transmittance value at 550 nm, ~97%, is achieved at the lowest OSR. The transmittance decreases with increasing OSR, reaching 95% at the highest OSR evaluated. The corresponding σ_{dc}/σ_{op} values (Fig. 4C) also decrease with increasing OSR. The σ_{dc}/σ_{op} ~ 50 was obtained for the film grown at the lowest OSR value of 140 ppm. The benchmark indicator of the commercial viability of transparent conductors, such as ITO corresponds to the σ_{dc}/σ_{op} value of ~35 (*2*, *8*, *46*). Howden *et al.* (*15*) and Lee *et al.* (*37*) reported the σ_{dc}/σ_{op} values of 12 and 14, respectively, in oCVD PEDOT films while using $FeCl_3$ as an oxidizing agent after HBr rinsing. The use of the volatile liquid oxidant ($VOCl_3$) used in this study not only represents a completely dry process by eliminating postdeposition rinsing (Fig. 1B) but also is responsible for the approximately fourfold improvement in σ_{dc}/σ_{op} (Fig. 4C) compared to its solid oxidant counterpart ($FeCl_3$).

An important influence on the optical properties of CPs is the optical bandgap (E_g), which is determined from the absorption spectra (fig. S6) using the Tauc relation (*48*)

$$\alpha h\nu = A(h\nu - E_g)^n \tag{10}$$

where α is the absorption coefficient, $h\nu$ is the photon energy, A is a constant, E_g is the optical bandgap, and n is the type of transition (here, n =1/2 for direct transition). Additional details on the calculation of E_g are provided in section S4.

The E_g values for the oCVD PEDOT films grown at the deposition temperature of 140°C systematically decreases from 2.9 to 2.6 eV as the OSR increases from 140 to 540 ppm due to an increase in the dopant level. The optical characteristics of conjugated polymers are primarily determined by the highest occupied molecular orbital (HOMO) and the lowest unoccupied molecular orbital (LUMO) energy levels. In general, the reduction of bandgap by an increase in dopant level is attributed to the destabilization of the HOMO than of the LUMO through donor-type substitution. It can be noted that the film with a wider bandgap exhibits higher transmittance (by comparing Fig. 4B and Fig. 4D) since only photons with energy higher than the bandgap can be absorbed. The smaller bandgap induces the lower transmittance and the larger absorption coefficient (ε), which increases the light absorption based on the Beer-Lambert relation; $A = \alpha cl$, where A, α,c, and l are absorption, absorption coefficient (molar absorptivity), concentration of sample, and path length,

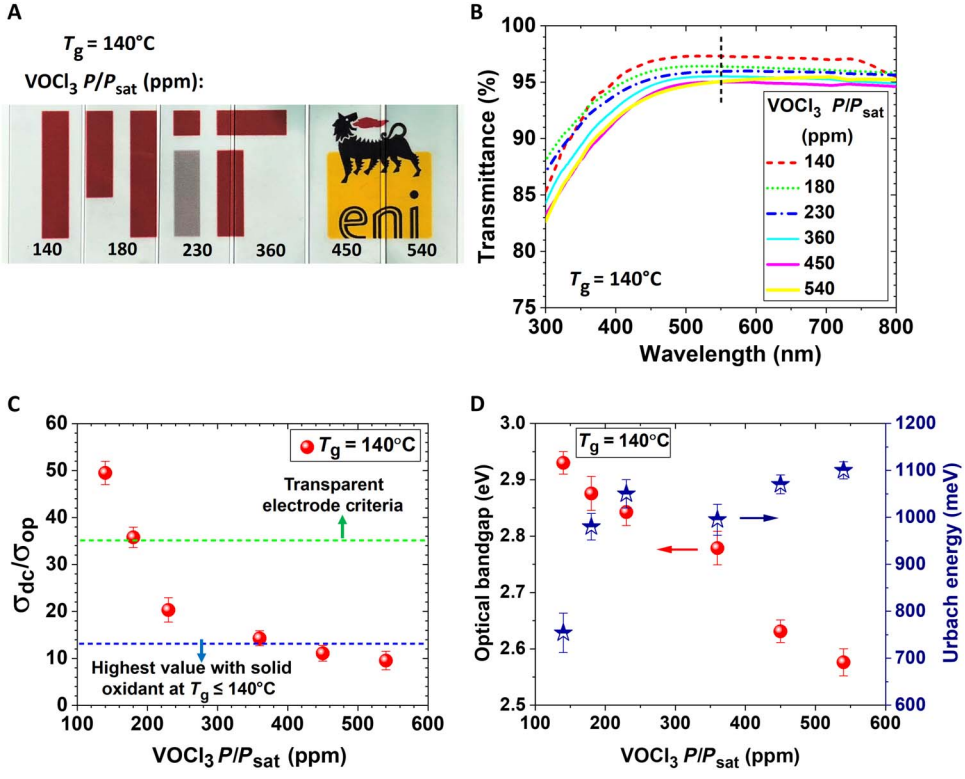

Fig. 4. The optical characteristics of PEDOT films. (**A**) Image of deposited PEDOT films on blank microscope glass slides (thickness of 1 mm) at different OSR. (**B**) The optical transmittance of PEDOT films grown at the deposition temperature of 140°C and different $VOCl_3$ saturation ratio in the visible regime ranging from 300 to 800 nm. (**C**) The FoM (FoM = σ_{dc}/σ_{op}, where σ_{dc} and σ_{op} are dc conductivity and optical conductivity, respectively) as a function of OSR in PEDOT films grown at the deposition temperature of 140°C. The blue and green dashed lines are the highest reported σ_{dc}/σ_{op} values in oCVD PEDOT films grown by $FeCl_3$ as an oxidant after acidic rinsing treatment and the benchmark indicator of the commercial viability of transparent conductors, respectively. (**D**) The optical bandgap and the Urbach energy values as a function of OSR for PEDOT films grown at the deposition temperature of 140°C.

respectively (*48*). The PEDOT films have a nondegenerate ground state that corresponds to a single geometric structure known as benzoid structure (the aromatic structure). The concentration of polarons increases with increase in dopant level and resulting in the formation of bipolarons (are spinless and doubly charged), which occupy distinct energy levels in the bandgap. It is postulated that the carrier mobility decreases at high carrier density due to the decrease in available unoccupied states. Therefore, for achieving high electrical conductivity, the threshold of doping should be considered. In this study, the oxidant level of 140 ppm yields the enhanced electrical conductivity due to the presence of pure face-on orientation and low *b*-axis lattice parameter.

The Urbach energy (E_U) is an indicator of the structural disorder in the material and can be derived from the following equation (*48*)

$$\alpha\,(h\vartheta) = \alpha_0 \exp\left(\frac{h\vartheta}{E_U}\right) \tag{11}$$

where α is an absorption coefficient, α_0 is a constant, $h\vartheta$ is the incident photon energy, and E_U is the Urbach energy of the localized states.

The dependence of ln(α) versus incident photon energy ($h\vartheta$) is exhibited in fig. S7 and provides information about the tail width of localized states in the bandgap. The higher E_U corresponds to the higher density of states in the bandgap. The E_U values for the PEDOT films grown at the deposition temperature of 140°C arise by increasing the OSR and correlate with an increase in the dopant level (Fig. 4D). The minimum (754 meV) and maximum (1100 meV) obtained E_U values correspond to the PEDOT films grown with the OSR value of 140 to 540 ppm, respectively. The less amount of E_U in film grown at the low OSR is related to better intercrystallite connection and lower disorder in the amorphous region.

To directly demonstrate the utility of the systematical optimized oCVD PEDOT, synthesized in a single step with $VOCl_3$ liquid oxidant, we fabricate inverted PSCs using oCVD PEDOT and commercial PEDOT:PSS as HTLs. Here, we selected a double-A cation perovskite composition with $Cs_{15}FA_{85}PbI_3$ formula due to its great absorption and excellent stability. Figure 5 (A and B) depicts the cross-sectional view scanning electron microscopy (SEM) image and the schematic of the PSC device based on oCVD PEDOT as the HTL. As seen, the inverted device consists of an ITO glass substrate coated by a thin layer of oCVD PEDOT (15 nm) as the HTL, a 450-nm-thick perovskite film as the absorber layer, a 23-nm-thick C60 as the electron transport layer (ETL), a 8-nm-thick bathocuproine (BCP) as the buffer layer, and a silver electrode with a thickness of 100 nm. Figure 5C shows the current density–voltage (*J-V*) curves of the best-performing PSC devices based on oCVD PEDOT and PEDOT:PSS (30 nm in thickness), measured under simulated AM1.5G solar irradiation under reverse bias. Notably, a minimum thickness of 30 nm for PEDOT:PSS is necessary to fabricate an efficient pinhole-free PSC without shorting; while using oCVD PEDOT, the pinhole-free PSC can be achieved with lower thicknesses of the HTL. Table 1 indicates that all the PV parameters of the PSC device based on oCVD PEDOT are improved as compared to the PEDOT:PSS control device. The statistics for the PV parameters of the PSCs based on PEDOT:PSS and oCVD PEDOT are shown in fig. S8. As seen, the average values of all PV parameters are enhanced for the oCVD PEDOT device compared to its counterpart, resulting in an improvement of the average PCE from 15.5 ± 0.70% to 17.2 ± 0.82%. To further confirm the J_{sc} of our devices, we measure the external quantum efficiency (EQE) of the corresponding devices as shown in Fig. 5D. The EQE of both devices are higher than 80% over the entire UV-vis region, yielding a calculated J_{sc} of 22.2 mA/cm^2 for the PEDOT:PSS device and 23.05 mA/cm^2 for oCVD PEDOT device. These J_{sc} values are in good agreement with the measured J_{sc} from *J-V* results.

It is worth pointing out that the PSC devices using these HTLs show a negligible *J-V* hysteresis. The statistic of the hysteresis indices (HIs) for the corresponding devices is shown in fig. S9. As can be observed in fig. S9, the average value of HI for the oCVD PEDOT device (0.8%) is slightly lower than the PEDOT:PSS device (0.87%). The thickness of oCVD PEDOT has a significant effect on the *J-V* results. The advantage of our CVD process is the fabrication of a very uniform layer of oCVD PEDOT with precise control on its thickness. To this effect, we fabricated PSC devices with different thicknesses of oCVD PEDOT, i.e., 15, 50, 130, and 200 nm, by adjusting the deposition time while keeping the OSR and growth temperature at the fixed values of 140 ppm and 140°C, respectively. The selection of OSR and growth temperature was based on obtaining higher electrical conductivity at lower OSR and higher growth temperature, which was discussed earlier. The variation of device performance as a function of the oCVD PEDOT film thickness is exhibited in fig. S10. As seen, the PCE of the PSC device dropped markedly by increasing the thickness of the HTL, mainly due to the lower transmittance in the thicker oCVD PEDOT HTL and, thus, the lower current density. Our results prove that a thin layer of oCVD PEDOT (~15 nm) is enough for fabrication of an efficient PSC device with PCE of more than 18% due to the uniformity and quality of oCVD PEDOT film, which is not the case for PEDOT:PSS.

The stability improvement is as significant as efficiency enhancement to make the PSCs ready for commercialization. To examine the stability of our PSC devices, we measure the shelf-life stability over 42 days. We kept the unencapsulated devices in ambient air with 20% relative humidity and measured them every 3 days. Figure 5E exhibits the results of the shelf-life stability test. As can be seen, the PSC with oCVD PEDOT maintains 76% of its initial PCE value after 42 days, which is much better than its counterpart device based on the PEDOT:PSS (37%). This result highlights the advantage of oCVD PEDOT as a more stable HTL in inverted PSC devices. The PCE deterioration in PSC with PEDOT:PSS HTL mainly originated from the degradation of the perovskite film and ITO by the highly acidic nature of PEDOT:PSS (*2*, *49*, *50*). Thus, replacement of PEDOT:PSS with a more stable HTL, i.e., oCVD PEDOT, can address this issue and markedly improve the stability of PSCs.

CONCLUSIONS

We have systemically investigated the structure of oCVD PEDOT films deposited at different growth temperatures and $VOCl_3$ saturation ratio. The GIXRD patterns revealed that the PEDOT films deposited at the higher growth temperatures and lower OSR result in an in situ reorganization to a face-on orientation. The ease of obtaining pure face-on orientation at temperatures compatible with plastic substrates (less than 140°C) with no need of postdeposition acidic rinsing step is the extraordinary advantage of using volatile liquid oxidant. In contrast, predominately edge-on orientation was previously reported with the solid oxidant $FeCl_3$ under similar oCVD process conditions, and a postdeposition rinsing step was required. The oCVD method enables simultaneously enhancing the charge transport in both intra- and intercrystallite by engineering the crystalline orientation and *b*-axis

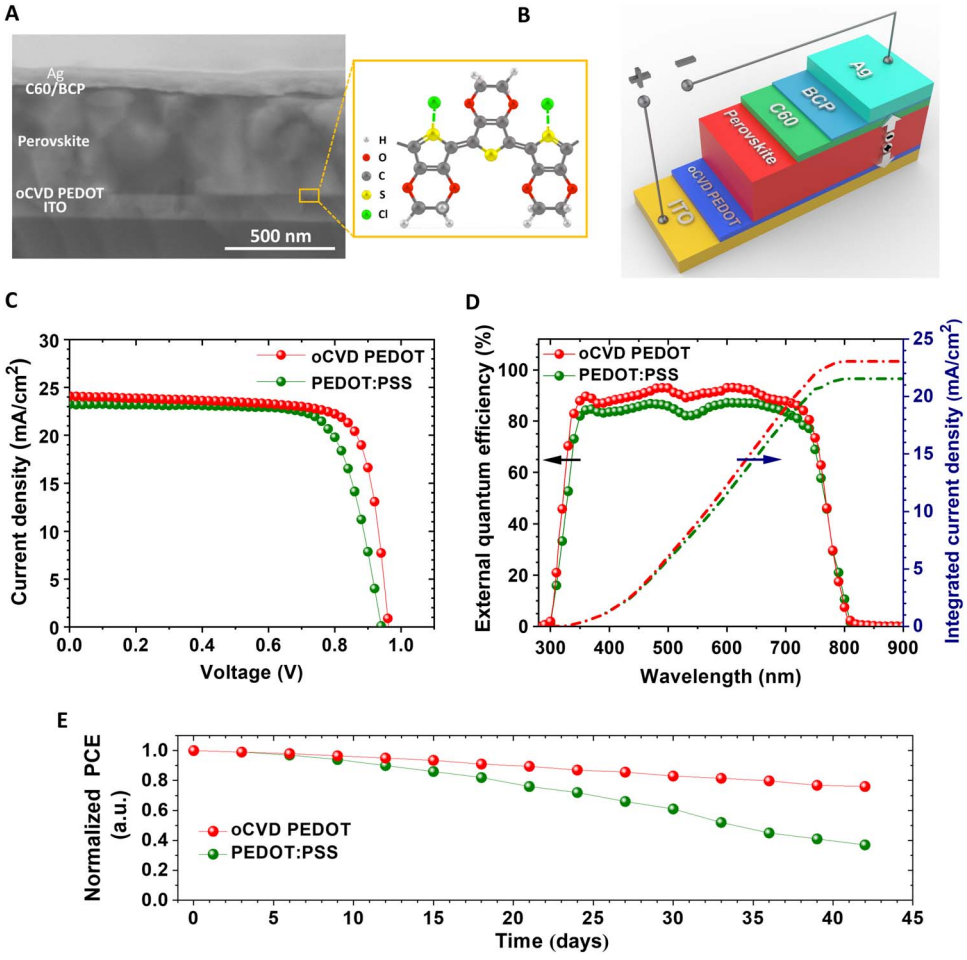

Fig. 5. PV characterization of PSC devices with oCVD PEDOT and PEDOT:PSS. (**A**) Cross-sectional SEM image and (**B**) schematic illustration of the device architecture for PSC device based on oCVD PEDOT HTL. (**C**) *J-V* curves and (**D**) EQE spectra and integrated current density of the PSCs fabricated on oCVD PEDOT and PEDOT:PSS HTLs. (**E**) The shelf-life stability performance of inverted PSCs with oCVD PEDOT and PEDOT:PSS HTLs. Notably, unencapsulated devices were kept in ambient air with 20% relative humidity, and the PCE was measured every 3 days.

Table 1. PV parameters of the best-performing PSCs with oCVD PEDOT and PEDOT:PSS HTLs. The PV features [open circuit voltage (V_{OC}), short circuit current density (J_{SC}), fill factor (FF), PCE, and J_{SC} estimated from EQE] of PSCs based on oCVD PEDOT and PEDOT:PSS HTLs.

	V_{oc} (V)	J_{sc} (mA/cm^2)	FF (%)	PCE (%)	J_{sc} from EQE
oCVD PEDOT	0.96	24.10	78	18.04	23.05
PEDOT:PSS	0.94	23.24	74	16.20	21.60

lattice parameter (π-π stacking distance). The higher degree of face-on orientation and the presence of lower *b*-axis lattice parameter in heavily doped films are indications of better intercrystallite and intracrystallite, respectively. Despite the fact that reducing the π-π stacking distance corresponds to the doping level reduction, higher overall in-plane conductivity is observed. We hypothesize that the geometrical constraints introduced by tighter π-π stacking result in increasing the occurrence of individual chains forming bridges across crystallites. In addition, the increased interchain charge transport results from reduced π-π stacking distances. This interchain transport creates bridges composed of multiple chains, capable of spanning longer distances for connecting more crystallites. The use of volatile liquid oxidant ($VOCl_3$) not only eliminates the acidic rinsing process but also exhibits approximately fourfold improvement in σ_{dc}/σ_{op} (obtained σ_{dc}/σ_{op} value of 50) and 10-fold enhancement in electrical conductivity (obtained conductivity of 2800 S/cm) compared to its solid oxidant counterpart ($FeCl_3$) at the deposition temperature compatible with plastic substrates. The optical bandgap of PEDOT films was systemically tuned in the range of 2.9 to 2.5 eV by adjusting the OSR. The high transmittance of 97% was achieved in film grown at the deposition temperature of 140°C and the lower OSR (higher bandgap value). Last, the oCVD PEDOT was exploited in the PSC as an HTL, and the maximum PCE of 18.04% was achieved compared to its PEDOT:PSS counterpart with the maximum PCE of 16.20%. The PSC device based on oCVD PEDOT not only exhibited higher PCE but also displayed approximately twofold higher stability compared to its PEDOT:PSS counterpart device. The PSC devices based on oCVD PEDOT and PEDOT:PSS retained 76 and 37% of its initial PCE values over 42 days, respectively, where the unencapsulated devices were kept in ambient air with 20% relative humidity.

MATERIALS AND METHODS

oCVD synthesis

A schematic illustration of the oCVD reactor with its components is shown in Fig. 1B. The EDOT monomer (purchased from Sigma-Aldrich) and $VOCl_3$ oxidant (purchased from Sigma-Aldrich) were placed in a temperature-controlled glass jar and fed simultaneously into the oCVD reactor through a heated line. The temperature of glass jars containing EDOT and $VOCl_3$ was kept at 140° and 30°C, respectively. The deposition time was kept constant (40 min) for all samples. The temperature of vapor delivery line (feed system) was controlled, and constant temperature over the entire length of the line was maintained to avoid internal condensation and decomposition of the vapor. The operating pressure of 1 torr during deposition was maintained and controlled using a throttle valve that is in communication with a baratron throughout the process. The PEDOT films were deposited on (100) Si wafers, ITO glass, and blank microscope glass slides. The oxidant reacted with monomers and created cation radicals on the growth surface, and then, pairs of cation radicals dimerized and deprotonated. In the following manner, dimers and trimers combined until the final CP film made up of *n*-mers was constructed in a step-growth polymerization fashion. The amount of EDOT flow rate was kept fixed at 12 SCCM (standard cubic centimeters per minute) at the different growth temperature of 110° and 140°C, while the flow rate of $VOCl_3$ varied. The total flow rate into the oCVD reactor was kept at a fixed value of 30 SCCM at each growth temperature using Ar gas flow as a balancer of total flow rate. The process details of calculating EDOT and $VOCl_3$ saturation ratios are provided in section S1, fig. S1, and table S1. After cooling down to room temperature under vacuum, the samples were taken out for material characterization and exploiting in device fabrication without any extra acidic solution treatment. The information related to material characterization methods (e.g., electrical conductivity measurement, GIXRD, SEM, XPS, optical characteristics including UV-vis–NIR analysis, and perovskite device characterization) is provided in section S1.

PSC device fabrication

ITO glasses were cleaned in the following baths respectively using ultrasonic Triton X-100 [1 volume % in deionized (DI) water], DI water, acetone, and isopropanol. All substrates were further cleaned by oxygen plasma for 5 min. After cleaning, the oCVD PEDOT films as an HTL were deposited on ITO glasses. PEDOT:PSS films were deposited on ITO glasses (for comparison purposes) by spin-coating at 2500 rpm for 45 s (ramp rate, 500 rpm/s), followed by annealing at 150°C for 20 min. Then, the $Cs_{15}FA_{85}PbI_3$ perovskite solution was prepared by dissolving CsCl [0.165 M; purchased from Tokyo Chemical Industry Co., Ltd. (TCI)], formamidinium iodide (0.935 M; purchased from Dyesol), PbI_2 (1.18 M; purchased from TCI), and 1 ml of mixed solvents of *N*,*N*-dimethylformamide:dimethyl sulfoxide (4:1) (volume ratio). The perovskite solution was heated up overnight at 60°C. For deposition, this solution was spin-coated in the following steps: (i) 1000 rpm for 10 s and (ii) 6000 rpm for 20 s (ramp rate, 2000 rpm/s). During the deposition process, 200 μl of chlorobenzene was dropped as an antisolvent 10 s right before end of spinning. Then, the films were annealed at 150°C for 30 min. The incorporated Cl ions in film by CsCl were removed during the annealing process. After cooling down, the films were transferred into an evaporation setup for ETL and electrode deposition. A 23-nm-thick C60 as an ETL, an 8-nm-thick BCP as a buffer layer, and a 100-nm-thick silver as an electrode were thermally evaporated on top of the perovskite films, respectively, to complete the device structure. The pressure of evaporation chamber was kept fixed at 10^{-6} torr during the deposition. The information related to device measurement is provided in section S1.

SUPPLEMENTARY MATERIALS

Supplementary material for this article is available at http://advances.sciencemag.org/cgi/content/full/5/11/eaay0414/DC1

Section S1. Methods and materials characterization
Section S2. Normalized integrated intensity based on LP factor, investigation of crystallite size, and lattice parameter
Section S3. Hopping probability by Miller-Abrahams model
Section S4. Optical bandgap (E_g) and Urbach energy (E_U) investigation
Table S1. The deposition parameters used in the growth of oCVD PEDOT films.
Table S2. The normalized integrated peak intensity of oCVD PEDOT films.
Table S3. The XPS elemental analysis of PEDOT films.
Table S4. The crystallite domain size in PEDOT films.
Table S5. The *a*-axis and *b*-axis lattice parameter information of PEDOT films.
Fig. S1. Saturation vapor pressure of monomer and oxidant at different temperatures.
Fig. S2. Thickness and deposition rate of PEDOT films as a function of process parameters.
Fig. S3. Effect of process parameters on the crystalline orientation of PEDOT films.
Fig. S4. The XPS analysis of PEDOT films.
Fig. S5. The effect of OSR on the *a*-axis lattice parameter of PEDOT films.
Fig. S6. The optical absorption spectra of PEDOT films.
Fig. S7. Urbach plot for PEDOT films.
Fig. S8. Statistics of the PV parameters for the PSCs with different HTLs.
Fig. S9. Statistics of HIs for the PSC devices.
Fig. S10. Variation of PSC device performance versus the thickness of oCVD PEDOT.

REFERENCES AND NOTES

1. K. K. Gleason, *CVD Polymers: Fabrication of Organic Surfaces and Devices* (John Wiley & Sons, 2015).
2. M. Heydari Gharahcheshmeh, K. K. Gleason, Device fabrication based on oxidative chemical vapor deposition (oCVD) synthesis of conducting polymers and related conjugated organic materials. *Adv. Mater. Interfaces* **6**, 1801564 (2019).
3. D. Evans, A bird's eye view of the synthesis and practical application of conducting polymers. *Polym. Int.* **67**, 351–355 (2018).
4. R. Brooke, P. Cottis, P. Talemi, M. Fabretto, P. Murphy, D. Evans, Recent advances in the synthesis of conducting polymers from the vapour phase. *Prog. Mater. Sci.* **86**, 127–146 (2017).
5. M. Wang, X. Wang, P. Moni, A. Liu, D. H. Kim, W. J. Jo, H. Sojoudi, K. K. Gleason, CVD polymers for devices and device fabrication. *Adv. Mater.* **29**, 1604606 (2017).
6. S. E. Atanasov, M. D. Losego, B. Gong, E. Sachet, J.-P. Maria, P. S. Williams, G. N. Parsons, Highly conductive and conformal poly(3,4-ethylenedioxythiophene) (PEDOT) thin films via oxidative molecular layer deposition. *Chem. Mater.* **26**, 3471–3478 (2014).
7. J. J. Kim, L. K. Allison, T. L. Andrew, Vapor-printed polymer electrodes for long-term, on-demand health monitoring. *Sci. Adv.* **5**, eaaw0463 (2019).
8. M. C. Barr, J. A. Rowehl, R. R. Lunt, J. Xu, A. Wang, C. M. Boyce, S. G. Im, V. Bulović, K. K. Gleason, Direct monolithic integration of organic photovoltaic circuits on unmodified paper. *Adv. Mater.* **23**, 3500–3505 (2011).
9. A. Liu, P. Kovacik, N. Peard, W. Tian, H. Goktas, J. Lau, B. Dunn, K. K. Gleason, Monolithic flexible supercapacitors integrated into single sheets of paper and membrane via vapor printing. *Adv. Mater.* **29**, 1606091 (2017).
10. P. Kovacik, G. D. Hierro, W. Livernois, K. K. Gleason, Scale-up of oCVD: Large-area conductive polymer thin films for next-generation electronics. *Mater. Horiz.* **2**, 221–227 (2015).
11. N. Cheng, L. Zhang, J. J. Kim, T. L. Andrew, Vapor phase organic chemistry to deposit conjugated polymer films on arbitrary substrates. *J. Mater. Chem. C* **5**, 5787–5796 (2017).
12. H. Goktas, X. Wang, N. D. Boscher, S. Torosian, K. K. Gleason, Functionalizable and electrically conductive thin films formed by oxidative chemical vapor deposition (oCVD) from mixtures of 3-thiopheneethanol (3TE) and ethylene dioxythiophene (EDOT). *J. Mater. Chem. C* **4**, 3403–3414 (2016).
13. A. Jaros, S. Bley, K. Zimmermann, L. Krieg, A. Castro-Carranza, J. Gutowski, F. Meierhofer, T. Voss, Optical properties and carrier dynamics in inorganic and hybrid inorganic/organic ZnO- and GaN-based nanowire structures. *Phys. Status Solidi B* **256**, 1800463 (2019).
14. L. Su, P. M. Smith, P. Anand, B. Reeja-Jayan, Surface engineering of a $LiMn_2O_4$ electrode using nanoscale polymer thin films via chemical vapor deposition polymerization. *ACS Appl. Mater. Interfaces* **10**, 27063–27073 (2018).

15. R. M. Howden, E. D. McVay, K. K. Gleason, oCVD poly(3,4-ethylenedioxythiophene) conductivity and lifetime enhancement via acid rinse dopant exchange. *J. Mater. Chem. A* **1**, 1334–1340 (2013).
16. S. G. Im, K. K. Gleason, Doping level and work function control in oxidative chemical vapor deposited poly (3,4-ethylenedioxythiophene). *Appl. Phys. Lett.* **90**, 152112 (2007).
17. H. Chelawat, S. Vaddiraju, K. Gleason, Conformal, conducting poly(3,4-ethylenedioxythiophene) thin films deposited using bromine as the oxidant in a completely dry oxidative chemical vapor deposition process. *Chem. Mater.* **22**, 2864–2868 (2010).
18. S. Nejati, T. E. Minford, Y. Y. Smolin, K. K. S. Lau, Enhanced charge storage of ultrathin polythiophene films within porous nanostructures. *ACS Nano* **8**, 5413–5422 (2014).
19. S. Kaviani, M. Mohammadi Ghaleni, E. Tavakoli, S. Nejati, Electroactive and conformal coatings of oxidative chemical vapor deposition polymers for oxygen electroreduction. *ACS Appl. Polym. Mater.* **1**, 552–560 (2019).
20. O. Bubnova, Z. U. Khan, H. Wang, S. Braun, D. R. Evans, M. Fabretto, P. Hojati-Talemi, D. Dagnelund, J.-B. Arlin, Y. H. Geerts, S. Desbief, D. W. Breiby, J. W. Andreasen, R. Lazzaroni, W. M. Chen, I. Zozoulenko, M. Fahlman, P. J. Murphy, M. Berggren, X. Crispin, Semi-metallic polymers. *Nat. Mater.* **13**, 190–194 (2014).
21. P. W. Anderson, Absence of diffusion in certain random lattices. *Phys. Rev.* **109**, 1492–1505 (1958).
22. O. Bubnova, X. Crispin, Towards polymer-based organic thermoelectric generators. *Energ. Environ. Sci.* **5**, 9345–9362 (2012).
23. N. Kim, B. H. Lee, D. Choi, G. Kim, H. Kim, J.-R. Kim, J. Lee, Y. H. Kahng, K. Lee, Role of interchain coupling in the metallic state of conducting polymers. *Phys. Rev. Lett.* **109**, 106405 (2012).
24. W. Nie, H. Tsai, R. Asadpour, J.-C. Blancon, A. J. Neukirch, G. Gupta, J. J. Crochet, M. Chhowalla, S. Tretiak, M. A. Alam, H. L. Wang, A. D. Mohite, High-efficiency solution-processed perovskite solar cells with millimeter-scale grains. *Science* **347**, 522–525 (2015).
25. Q. Chen, N. D. Marco, Y. Yang, T.-B. Song, C.-C. Chen, H. Zhao, Z. Hong, H. Zhou, Y. Yang, Under the spotlight: The organic–inorganic hybrid halide perovskite for optoelectronic applications. *Nano Today* **10**, 355–396 (2015).
26. M. M. Tavakoli, R. Tavakoli, P. Yadav, J. Kong, A graphene/ZnO electron transfer layer together with perovskite passivation enables highly efficient and stable perovskite solar cells. *J. Mater. Chem. A* **7**, 679–686 (2019).
27. K. E. Aasmundtveit, E. J. Samuelsent, L. A. A. Pettersson, O. Inganäs, T. Johansson, R. Feidenhans'l, Structure of thin films of poly(3,4-ethylenedioxythiophene). *Synth. Met.* **101**, 561–564 (1999).
28. L. E. Alexander, *X-Ray Diffraction Methods In Polymer Science* (Wiley Series on the Science and Technology of Materials, John Wiley & Sons, 1969).
29. X. Wang, X. Zhang, L. Sun, D. Lee, S. Lee, M. Wang, J. Zhao, Y. Shao-Horn, M. Dincă, T. Palacios, K. K. Gleason, High electrical conductivity and carrier mobility in oCVD PEDOT thin films by engineered crystallization and acid treatment. *Sci. Adv.* **4**, eaat5780 (2018).
30. A. Ugur, F. Katmis, M. Li, L. Wu, Y. Zhu, K. K. Varanasi, K. K. Gleason, Low-dimensional conduction mechanisms in highly conductive and transparent conjugated polymers. *Adv. Mater.* **27**, 4604–4610 (2015).
31. D. Gargi, R. J. Kline, D. M. DeLongchamp, D. A. Fischer, M. F. Toney, B. T. O'Connor, Charge transport in highly face-on poly(3-hexylthiophene) films. *J. Phys. Chem. C* **117**, 17421–17428 (2013).
32. J. Rivnay, M. F. Toney, Y. Zheng, I. V. Kauvar, Z. Chen, V. Wagner, A. Facchetti, A. Salleo, Unconventional face-on texture and exceptional in-plane order of a high mobility n-type polymer. *Adv. Mater.* **22**, 4359–4363 (2010).
33. L. H. Jimison, M. F. Toney, I. McCulloch, M. Heeney, A. Salleo, Charge-transport anisotropy due to grain boundaries in directionally crystallized thin films of regioregular poly(3-hexylthiophene). *Adv. Mater.* **21**, 1568–1572 (2009).
34. S. D. Kang, G. J. Snyder, Charge-transport model for conducting polymers. *Nat. Mater.* **16**, 252–257 (2017).
35. R. Noriega, J. Rivnay, K. Vandewal, F. P. V. Koch, N. Stingelin, P. Smith, M. F. Toney, A. Salleo, A general relationship between disorder, aggregation and charge transport in conjugated polymers. *Nat. Mater.* **12**, 1038–1044 (2013).
36. P. Moni, J. Lau, A. C. Mohr, T. C. Lin, S. H. Tolbert, B. Dunn, K. K. Gleason, Growth temperature and electrochemical performance in vapor deposited poly(3,4-ethylenedioxythiophene) thin films for high rate electrochemical energy storage. *ACS Appl. Energy Mater.* **1**, 7093–7105 (2018).
37. S. Lee, D. C. Paine, K. K. Gleason, Heavily doped poly(3,4-ethylenedioxythiophene) thin films with high carrier mobility deposited using oxidative CVD: Conductivity stability and carrier transport. *Adv. Funct. Mater.* **24**, 7187–7196 (2014).
38. B. D. Cullity, in *Elements of X-ray Diffraction* (Addison-Wesley, 1978), pp. 81–143.
39. A. J. Heeger, Nobel lecture: Semiconducting and metallic polymers: The fourth generation of polymeric materials. *Rev. Mod. Phys.* **73**, 681–700 (2001).
40. G. Tzamalis, N. A. Zaidi, C. C. Homes, A. P. Monkman, Doping-dependent studies of the Anderson-Mott localization in polyaniline at the metal-insulator boundary. *Phys. Rev. B* **66**, 085202 (2002).
41. D. Jérome, A. Mazaud, M. Ribault, K. Bechgaard, Superconductivity in a synthetic organic conductor $(TMTSF)_2PF_6$. *J. Phys. Lett.* **41**, 95–98 (1980).
42. V. Coropceanu, J. Cornil, D. A. da Silva Filho, Y. Olivier, R. Silbey, J.-L. Brédas, Charge transport in organic semiconductors. *Chem. Rev.* **107**, 926–952 (2007).
43. R. A. Marcus, N. Sutin, Electron transfers in chemistry and biology. *Biochim. Biophys. Acta* **811**, 265–322 (1985).
44. W.-Q. Deng, W. A. Goddard, Predictions of hole mobilities in oligoacene organic semiconductors from quantum mechanical calculations. *J. Phys. Chem. B* **108**, 8614–8621 (2004).
45. A. Miller, E. Abrahams, Impurity conduction at low concentrations. *Phys. Rev.* **120**, 745–755 (1960).
46. V. Scardaci, R. Coull, J. N. Coleman, Very thin transparent, conductive carbon nanotube films on flexible substrates. *Appl. Phys. Lett.* **97**, 023114 (2010).
47. A. W. Lang, Y. Li, M. D. Keersmaecker, D. E. Shen, A. M. Österholm, L. Berglund, J. R. Reynolds, Transparent wood smart windows: Polymer electrochromic devices based on poly(3,4-ethylenedioxythiophene):poly(styrene sulfonate) electrodes. *ChemSusChem* **11**, 854–863 (2018).
48. J. Tauc, A. Menth, States in the Gap. *J. Non Cryst. Solids* **8**, 569–585 (1972).
49. W. J. Jo, J. T. Nelson, S. Chang, V. Bulović, S. Gradecak, M. S. Strano, K. K. Gleason, Oxidative chemical vapor deposition of neutral hole transporting polymer for enhanced solar cell efficiency and lifetime. *Adv. Mater.* **28**, 6399–6404 (2016).
50. J. C. Yu, J. A. Hong, E. D. Jung, D. B. Kim, S.-M. Baek, S. Lee, S. Cho, S. S. Park, K. J. Choi, M. H. Song, Highly efficient and stable inverted perovskite solar cell employing PEDOT:GO composite layer as a hole transport layer. *Sci. Rep.* **8**, 1070 (2018).

Acknowledgments

Funding: We acknowledge the financial support of the Eni S.p.A. under the Eni-MIT Alliance Solar Frontiers Program. **Author contributions:** M.H.G. synthesized the oCVD PEDOT thin films, performed electrical conductivity, GIXRD, SEM, XPS, UV-vis–NIR measurements, and carried out nanostructural engineering of oCVD PEDOT based on dopant level under the supervision of K.K.G. M.M.T. carried out PSC device characterization and worked with M.H.G. on optimizing the solar cell device performance under the supervision of J.K. E.F.G. provided technical oCVD reactor design and worked with M.H.G. for adjusting the reactor based on the installation of liquid oxidant delivery line under the supervision of K.K.G. M.T.R. assisted in PEDOT fabrication and characterization under the supervision of K.K.G. K.K.G. and J.K. directed the research and supervised this project. M.H.G. and K.K.G. prepared the manuscript. All authors contributed to the manuscript. **Competing interests:** The authors declare that they have no competing interests. **Data and materials availability:** All data needed to evaluate the conclusions in the paper are present in the paper and/or the Supplementary Materials. Additional data related to this paper may be requested from the authors.

Submitted 14 May 2019
Accepted 23 September 2019
Published 22 November 2019
10.1126/sciadv.aay0414

Citation: M. Heydari Gharahcheshmeh, M. M. Tavakoli, E. F. Gleason, M. T. Robinson, J. Kong, K. K. Gleason, Tuning, optimization, and perovskite solar cell device integration of ultrathin poly(3,4-ethylene dioxythiophene) films via a single-step all-dry process. *Sci. Adv.* **5**, eaay0414 (2019).